Article

Probing Interfacial Interactions in Ternary Nanocomposites of Ti₃C₂Tₓ MXene Nanoplatelets, Multiwalled Carbon Nanotubes, and Poly(vinyl alcohol) toward Synergistic Reinforcement

Ming Dong, Yi Hu, Xiangyan Yu, Mufeng Liu, Emiliano Bilotti, Han Zhang, and Dimitrios G. Papageorgiou*
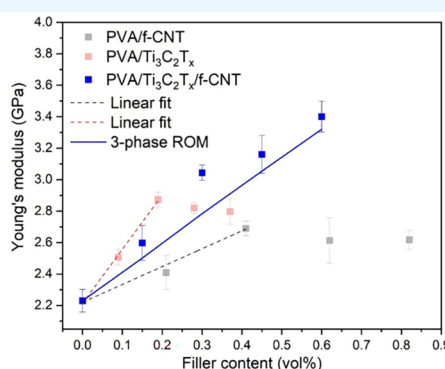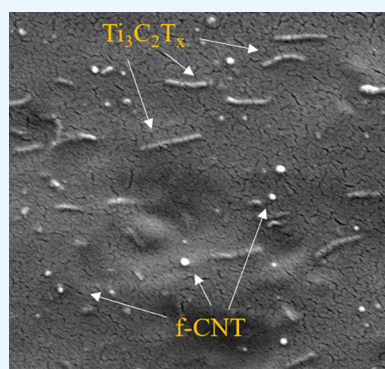
Read Online

ACCESS | lill Metrics & More | Article Recommendations | SI Supporting Information

ABSTRACT: The fabrication of ternary nanocomposites has been proven to be a successful method to achieve synergistic reinforcement resulting from the combination of nanofillers within a polymer matrix. In this study, Ti₃C₂Tₓ MXene nanoplatelets and functionalized multiwalled carbon nanotubes (f-CNTs) were combined to prepare ternary poly(vinyl alcohol) (PVA) nanocomposites. The Ti₃C₂Tₓ MXene/f-CNT hybrids were cross-linked through hydrogen bonds, which promoted homogeneous dispersion of the nanofillers and enabled strong interfacial interactions between the nanofillers and the PVA matrix. Compared to pure PVA, Young's modulus and the tensile strength of the nanocomposites with only 1.2 wt % of MXene/f-CNT hybrids were improved by about 52% and 48%, respectively. The ternary nanocomposites display synergistic effects as revealed by micromechanics and stress-induced Raman band shifts. The *in situ* Raman deformation studies allowed the observation of more effective stress transfer in the nanocomposites due to hydrogen bonds between the hybrids and the matrix that ultimately prevented the formation of aggregates.

KEYWORDS: Ti₃C₂Tₓ MXene, carbon nanotube, poly(vinyl alcohol), mechanical properties, synergistic mechanism

1. INTRODUCTION

The past decade has seen a surge of research in polymer nanocomposites. Some of the most-researched nanofillers include carbon nanotubes (CNTs) and graphene-related 2D materials,[1−3] which exhibit superior intrinsic properties, allowing them to be employed in high-end applications that require excellent performance and multifunctionality. However, a number of challenges are faced when such nanomaterials are introduced within polymers, including poor interfacial interactions and formation of agglomerates, which limit performance and are known to act as failure points.[4] The surface functionalization of nanofillers can simultaneously address both issues but can also induce defects to the nanocrystalline structures of the nanofillers and therefore lead to inferior intrinsic properties.

Recently, MXenes, a class of transition metal carbides and nitrides, have been used as reinforcements in polymers. They display a multitude of surface functional groups, such as −O, −OH, and −F that facilitate polymer/filler interfacial bonding; nevertheless, they can still provide exceptional conductivity to impart multifunctional properties for the end nanocomposites.[5−8] This can address issues with graphene-related materials, whose conductivity is subject to significant reduction when functionalization is used to enhance the strength of the polymer/filler interfaces.[9−12]
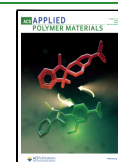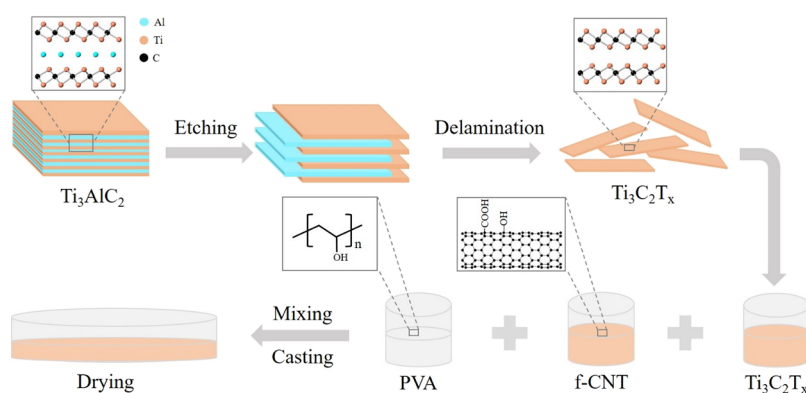
Figure 1. Schematic diagram of the preparation of PVA/Ti$_3$C$_2$T$_x$/f-CNT nanocomposites.

Another interesting aspect of polymer nanocomposites includes the observation that the combination of two or more different types of nanofillers may induce synergistic effects, without affecting much the processability of the final nanocomposites.[13−16] The emergence of synergistic effects in composite materials is intricately connected to several factors. First, it is influenced by the geometry of the fillers incorporated into the composite. Second, the structure of hybrid fillers, which can consist of a combination of different materials, plays a pivotal role in determining these effects. Finally, the interactions occurring at the interfaces between these hybrid fillers and the polymer matrix further contribute to and define the nature of the synergistic phenomena in the composite. Understanding these interrelated aspects is essential for tailoring composite materials with enhanced properties and performance.[17,18] An efficient approach to design hybrid filler systems is to use a 1D nanomaterial in combination with a 2D nanomaterial. For instance, graphene oxide (GO) and CNTs have been combined to improve the mechanical and electrical properties of polymer nanocomposites.[19−22] Hybrid fillers are typically bonded by $\pi-\pi$ interactions,[23] hydrogen bonds,[24] and covalent bonds,[25] resulting in the formation of 3D structures with increased contact area between nanofillers and polymer matrices. In this way, hybrid nanocomposites display functional properties that can outperform single filler systems with even lower optimal filler loadings.[26] Additionally, the issue of agglomeration may be mitigated when the fillers are in different shapes which can lead to lower percolation.[27] Recently, MXenes have been combined with CNTs to improve the mechanical and electrical properties of polymer nanocomposites.[28,29] However, the synergistic mechanism and the interfacial interactions of such composites have not been studied in detail.

In this work, ternary nanocomposites were fabricated using MXene and CNTs to reinforce a PVA matrix. Ti$_3$C$_2$T$_x$ MXene nanoplatelets were synthesized *in situ* by HF etching while CNTs were oxidized by a H$_2$SO$_4$/HNO$_3$ mixture. The PVA nanocomposites were prepared by a facial casting method, and the abundance of hydroxyl groups in PVA structure was expected to facilitate interfacial interactions with MXene nanoplatelets and f-CNTs. Mechanical properties of the nanocomposites were evaluated by tensile testing and analyzed by the rule of mixtures. The synergistic reinforcing mechanism has been studied by means of micromechanics, and the interfacial stress transfer mechanism was studied by *in situ* strain-induced Raman band shifts. This work provides a fundamental insight into the micromechanics of MXene-based

hybrid nanocomposites, essential for the development of multifunctional nanocomposites to be used in structural components, energy storage devices, and e-wearables.

2. EXPERIMENTAL SECTION

2.1. Materials. The Ti$_3$AlC$_2$ MAX powders (particle size of 38 μm, purity of 98%) were procured from Jilin 11 Technology Co., Ltd. Lithium fluoride (LiF, 98.5% grade) powder, hydrochloric acid (HCl, ACS reagent), concentrated nitric acid (HNO$_3$, 68%), and sulfuric acid (H$_2$SO$_4$) were purchased from Sigma-Aldrich. Conductive multiwalled carbon nanotubes with an inner diameter of 3−5 nm, outer diameter of 8−15 nm, length of 3−12 μm, and purity >95 wt % were purchased from Shenzhen Liguangrun E-commerce Co., Ltd. The PVA powder with average molecular weight of 67,000 was provided by ME Scientific Engineering Ltd.

2.2. Synthesis of Ti$_3$C$_2$T$_x$ MXene Nanoplatelets. Ti$_3$C$_2$T$_x$ MXene nanoplatelets were prepared by the *in situ* HF etching method.[30] First, 1.6 g of LiF was added to 20 mL of 9 M HCl in a PTFE beaker while stirring for 30 min to prepare the etchant. After that, 1 g of Ti$_3$AlC$_2$ MAX powder was dissolved in the etchant and the reaction was allowed to run at 40 °C for 24 h under continuously stirring. The obtained Ti$_3$C$_2$T$_x$ slurry was washed with DI water by centrifuging at 3500 rpm for 5 min each cycle, until its pH reached 6− 7. Then, the Ti$_3$C$_2$T$_x$ slurry was redispersed in DI water and bath sonicated under Ar flow for 10 min to obtain monolayer or fewlayer Ti$_3$C$_2$T$_x$. The mixture was centrifuged at 3500 rpm for 20 min to obtain a Ti$_3$C$_2$T$_x$ MXene suspension. The concentration of the suspension was determined to be ~3 mg/mL by vacuum filtering a certain amount of suspension through a membrane (mixed cellulose ester, pore size 0.22 μm).

2.3. Oxidation of Multiwalled Carbon Nanotubes. Functionalization of CNTs was carried out using acidic oxidation.[31] Briefly, 0.3 g of the pristine CNTs (p-CNTs) was dispersed in 25 mL of a 3:1 ratio H$_2$SO$_4$/HNO$_3$ mixture. The dispersion was achieved by magnetic stirring at 100 °C for 6h. After cooling to room temperature, the mixture was diluted and washed with deionized (DI) water until the pH was neutral. The sample was then dried at 40 °C under vacuum overnight to obtain functionalized CNTs (f-CNTs from now on).

2.4. Preparation of PVA/Ti$_3$C$_2$T$_x$/f-CNT Nanocomposites. The solution blending method was used to prepare PVA/Ti$_3$C$_2$T$_x$/f-CNT nanocomposites as illustrated in Figure 1. A certain amount of PVA powder was dispersed in DI water at 90 °C to prepare a 5 wt % PVA aqueous solution. The f-CNT powder was also dispersed in DI water by bath sonication (15 min) to give a 0.5 mg/mL solution. The synthesized MXene suspension with a concentration of 3 mg/mL was then diluted to 0.5 mg/mL. After that, the PVA aqueous solution was mixed with MXene and f-CNT suspensions to prepare nano-composites with different filler loadings (0.3, 0.6, 0.9, and 1.2 wt %). The weight ratio of f-CNT to MXene nanoparticles was 1/1. The mixtures were untrasonicated for 15 min and further stirred for 60 min to disperse the fillers uniformly in the PVA matrix. The mixtures
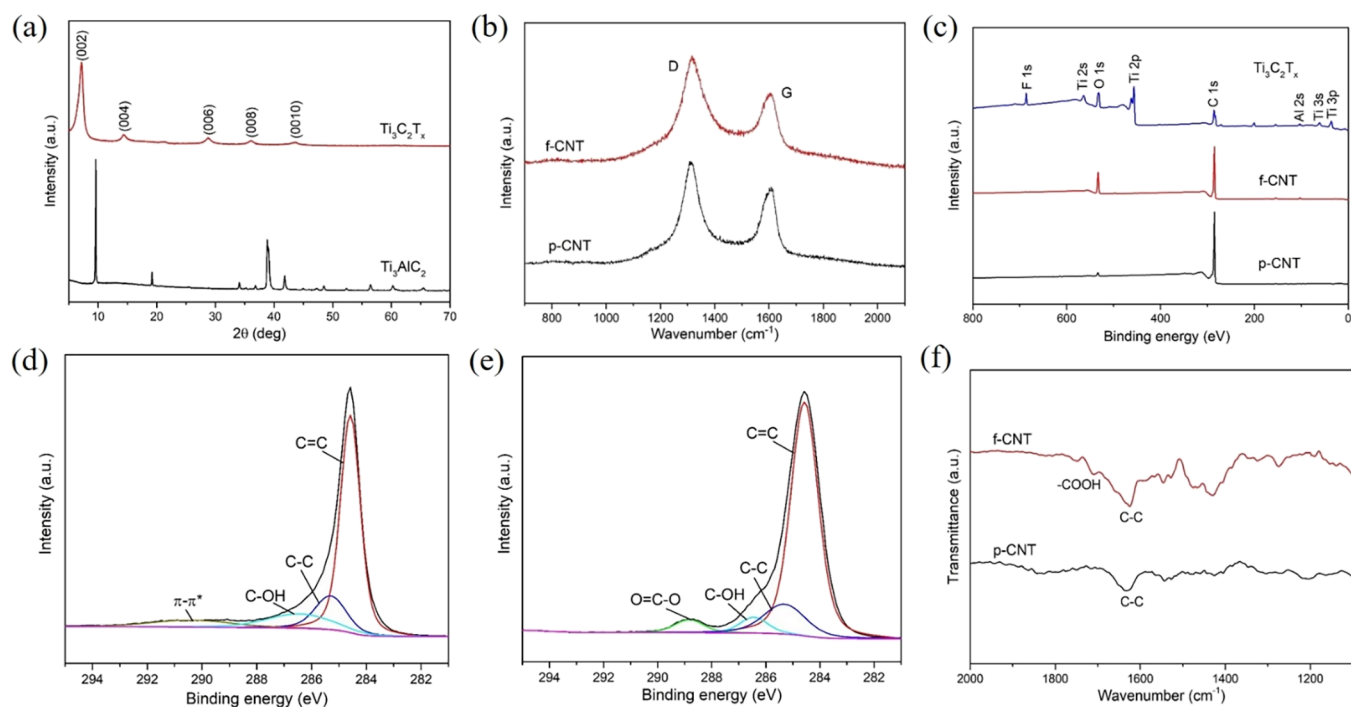
Figure 2. (a) XRD patterns of Ti_3AlC_2 MAX and $Ti_3C_2T_x$ MXene. (b) Raman spectra of p-CNT and f-CNT. (c) XPS spectra of $Ti_3C_2T_x$ MXene, p-CNT, and f-CNT. XPS C 1s peaks of (d) p-CNT and (e) f-CNT. (f) FTIR spectra of p-CNT and f-CNT.

were then poured into Petri dishes and dried in an oven at 60 °C for 24 h. A few drops of the mixtures (20 μL) were also casted onto PMMA beams to dry for *in situ* Raman measurements.

2.5. Characterization. X-ray diffraction (XRD) was carried on an ANalytical X'Pert-Pro diffractometer with a Cu–Kα radiation source. The scan was operated in 5–70° 2θ geometry on reflection mode. X-ray photoelectron spectroscopy (XPS) was carried out in an ultrahigh-vacuum system using a ThermoFisher Nexsa X-ray photoelectron spectrometer. The chemical compositions of p-CNT, f-CNT, and $Ti_3C_2T_x$ powders were analyzed. The microstructures of exfoliated MXene, f-CNT, and the fracture surfaces of composites were observed using scanning electron microscopy (SEM, FEI Inspect-F, The Netherlands) with an acceleration voltage of 5 kV. A few drops of MXene-, f-CNT-, and MXene/f-CNT-based solutions were deposited on a silicon wafer and dried at room temperature. The nanocomposites were cryo-fractured after immersion in liquid N_2. The thickness, height profile, and aspect ratio of MXene and f-CNT samples were characterized by atomic force microscopy (AFM) in semicontact mode. Differential scanning calorimetry (DSC) measurements of the composite films were conducted by a TA DSC 25 under an Ar flow of 20 mL/min, and the samples were heated at a rate of 10 °C/min from 10 to 280 °C. The samples were held at 280 °C for 5 min, cooled down to room temperature at 50 °C/min, and then reheated at 10 °C/min to record the melting point. Fourier transform infrared spectroscopy (FTIR) was performed by using a Smart iTX Optical Base, AR Diamond Crystal Plate for Smart iTX and X700. The scanning range was 4000–500 cm^{-1} and the resolution was 4 cm^{-1}. The tensile properties of pure PVA and its nanocomposites were tested by using an Instron 5900R84 machine. The films were cut into a dogbone shape with a gauge length of 10 mm and a width of 3 mm. The thickness of the samples was about 0.05 mm. The load cell was 100 N and the loading rate was 1 mm/min. Raman spectra were collected by using a micro-Raman spectrometer (Renishaw inVia) in a backscattering configuration. The laser excitation of 785 nm with a grating of 1200 grooves/mm was used to record the Raman signal. The laser power was kept below 1 mW to avoid heating effects. For the *in situ* Raman deformation study, the PMMA beam with PVA composite films (described in Section 2.4) was deformed by using a four-point bending device, which was adjusted on the microscope

stage.[32−34] A strain gauge was attached to the center of the beam to monitor strain. Strain was applied to the specimens in steps of about 0.05% and three spectra were recorded and averaged at each strain level. For polarized Raman spectroscopy, VV (vertical/vertical) polarization, where the incident and scattered polarizations were the same, was used. The setup of polarized Raman spectroscopy can be found in previous studies.[32,35] The film was rotated in steps of 10°.

3. RESULTS AND DISCUSSION

3.1. Primary Characterization of $Ti_3C_2T_x$ MXene and CNTs. Figure 2a illustrates the XRD spectra of Ti_3AlC_2 MAX and $Ti_3C_2T_x$ MXene. Clearly, the (104) peak of Ti_3AlC_2 at $2\theta \approx 39°$ disappeared after etching, indicating almost complete removal of the Al element. The (002) peak of Ti_3AlC_2 shifted to smaller angles and broadened, suggesting an increase in the d-spacing due to the presence of Li^+. For $Ti_3C_2T_x$ MXene, four more peaks were observed corresponding to (004), (006), (008), and (0010) crystal planes. Figure S1 shows the Raman spectra of Ti_3AlC_2 MAX and $Ti_3C_2T_x$ MXene in the range of 100−800 cm^{-1}. It can be seen that the A_{1g} (Ti, Al) referred to the ω_4 peak of MAX moved to lower wavenumber as the Al element was etched and C and surface groups were involved.[36] Another out-of-plane peak, ω_6, moved to a higher wavenumber. Overall, the differences in XRD and Raman spectra indicate the removal of Al and the successful synthesis of MXene nanoplatelets. Figure 2b shows the Raman spectra of p-CNT and f-CNT in the range of 800−2000 cm^{-1}. Two peaks corresponding to the D-band and G-band of CNTs were observed for both pristine and acid-treated materials. The D-band located at ∼1311 cm^{-1} is an indication of structural defects, and the G-band located at ∼1600 cm^{-1} represents the in-plane vibration of the sp^2 bonds.[37] The effects of acidic oxidation can be estimated from the intensity ratio of the D-band to the G-band (I_D/I_G), which is an indication of the degree of defects. For p-CNT, the I_D/I_G ratio was 1.70, which implies that there is a small degree of defectiveness for the as-
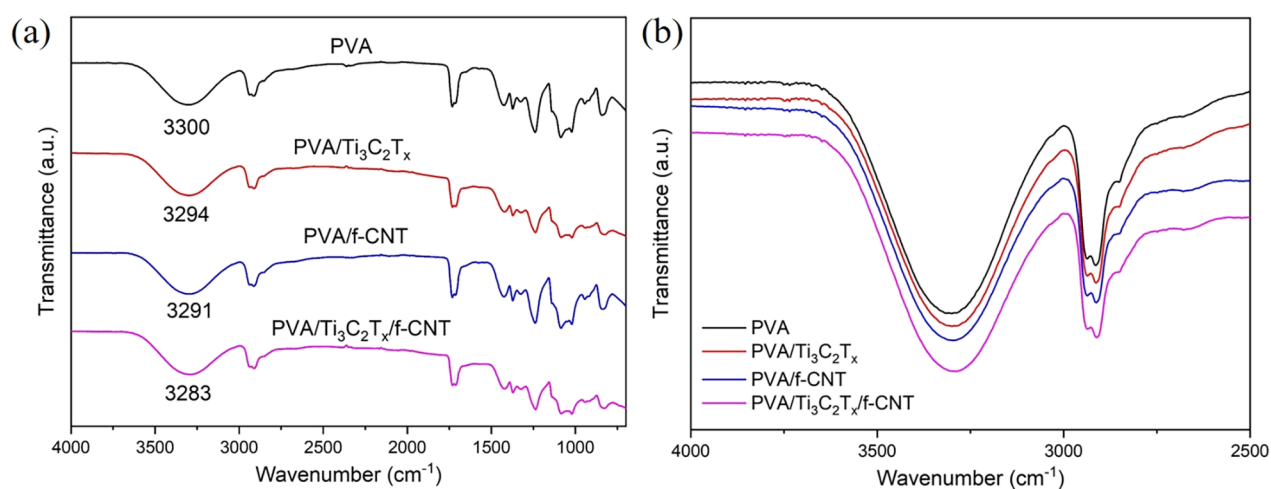
Figure 3. (a, b) FTIR of pure PVA, PVA/f-CNT, PVA/Ti$_3$C$_2$T$_x$ and PVA/Ti$_3$C$_2$T$_x$/f-CNT nanocomposites. The filler loadings are 1.2 wt % for f-CNT, Ti$_3$C$_2$T$_x$, and Ti$_3$C$_2$T$_x$/f-CNT.

received samples. After acid treatment, the ratio of I_D/I_G increased to 2.26. This indicates that defects were introduced during the oxidation process of CNTs. The acid functionalization process is beneficial for the dispersion of CNTs in solvent and the interfacial interaction between CNTs and the matrix (i.e., −COOH grafting).[38]

The oxidation behavior can be further analyzed by XPS as shown in Figure 2c. The p-CNT and f-CNT spectra show C 1s and O 1s peaks. There are large differences in the carbon and oxygen atomic percentages in p-CNT and f-CNT. The C/O ratio of p-CNT was 97.05/2.53, and the ratio increased to 81.96/15.16 for f-CNT. This is attributed to the grafting of carboxylic and hydroxyl functions onto the CNT surfaces by acid oxidation.[39] The C 1s peaks of p-CNT and f-CNT are shown in Figure 2d,e. For both types of nanotubes, the C=C peak at 284.6 eV, the C−C peak at 285.3 eV, and the C−OH peak at 286.4 eV were observed. For p-CNT, the $\pi-\pi^*$ peak at 290.4 eV was observed. This peak was not observed in f-CNT, most probably due to acid washing.[31] For f-CNT, an additional peak of the O=C−O ratio at 288.8 eV was observed, which confirmed the presence of carboxylic acid groups. The XPS spectra of Ti$_3$C$_2$T$_x$ is also shown in Figure 2c. The peaks observed at 285.7 eV, 532.2 and 686.1 eV were assigned to C 1s, O 1s, and F 1s, respectively, and the peaks observed at 36.4, 60.6, 457.0, and 562.7 eV were attributed to Ti 3p, Ti 3s, Ti 2p, and Ti 2s, respectively.[40] The analysis also confirmed the presence of a very small amount of aluminum (evidenced by peaks at 103 and 154 eV), originating from the residual material after the etching process.[41]

Finally, FTIR was used to characterize the functional groups on the surfaces of p-CNT and f-CNT (Figure 2f). For both types of CNTs, the C−C stretching vibration was observed at ~1630 cm^{-1}. An extra peak appeared at ~1711 cm^{-1} for f-CNT, which was ascribed to the −COOH stretching vibration.[39] This further confirmed that carboxylic acid was formed on the surface of the f-CNT. The XRD patterns of p-CNT and f-CNT are shown in Figure S2 (Supporting Information). There is no significant difference between the two patterns. Two characteristic peaks at 2θ = 25.84° and 43.49° corresponding to reflections from the (002) and (004) planes were observed for both tubes. The sharpness of the peak at (002) indicates that the graphitic structure of f-CNTs was preserved, and there is no significant structural damage on the

nanotubes after acidic treatment. The crystallinity remained almost the same as any decrease would be indicated by broader peaks and diffraction peak shifts toward lower angles.[42]

The SEM images of exfoliated Ti$_3$C$_2$T$_x$ MXenes and acid-treated CNTs are shown in Figure S3a-b. After etching and delamination, bulk MAX precursors were exfoliated to thin and flat MXene nanoplatelets (Figure S3a). The lateral size of the MXene nanoplatelets ranged from 1 to 3 μm. Regarding acid-treated CNTs, their length ranges from hundreds of nanometers to several microns. An SEM image of Ti$_3$C$_2$T$_x$/f-CNT hybrid nanoparticles is shown in Figure S3c, where the hybrids appear stacked together and adhered to each other. This is induced by the strong interfacial and electrostatic interactions between the nanofillers, leading to stacking and aggregation during the drying process. A representative AFM image and the height profile of the produced MXene nanoplatelets are shown in Figures S 3d-e. In addition, Figures S 3f-g show the statistics of the lateral size (3.15 ± 1.23 μm) and thickness (2.75 ± 1.12 nm) after studying more than 60 individual MXene nanoplatelets. The aspect ratio of MXene nanoplatelets was calculated to be 1145. The length and thickness of f-CNTs are on the order of 1.27 ± 0.65 μm (Figure S3h) and 11.94 ± 2.07 nm (Figure S3i), respectively. The aspect ratio of f-CNTs was therefore calculated to be 106.

3.2. Microstructure of PVA/Ti$_3$C$_2$T$_x$/f-CNT Films. The interactions between the PVA matrix and fillers were investigated by FTIR as shown in Figure 3a. The two peaks in the 1000−1200 cm^{-1} region for pure PVA correspond to the C−O vibration of C−OH groups.[43] The peak located at around 3300 cm^{-1} was ascribed to the stretching vibration of −OH groups. This peak moved to 3291 cm^{-1} for 1.2 wt % f-CNT/PVA film and 3294 cm^{-1} for 1.2 wt % Ti$_3$C$_2$T$_x$/PVA film. This indicates that additional hydrogen bonding formed after the interaction of PVA with the individual fillers. This peak moved to a lower wavenumber (3283 cm^{-1}) for 1.2 wt % Ti$_3$C$_2$T$_x$/f-CNT/PVA film (Figure 3b). Evidently, robust hydrogen bonds were formed between PVA and Ti$_3$C$_2$T$_x$/f-CNT hybrids.[43] The interfacial interactions between Ti$_3$C$_2$T$_x$ and f-CNT were also characterized by FTIR, as shown in Figure S4 of the Supporting Information. The peaks at 3395 cm^{-1} for Ti$_3$C$_2$T$_x$ and 3442 cm^{-1} for f-CNT can be assigned to the stretching vibration of the hydrogen bonded hydroxyl (−OH) group. This peak moved to 3421 cm^{-1} for the
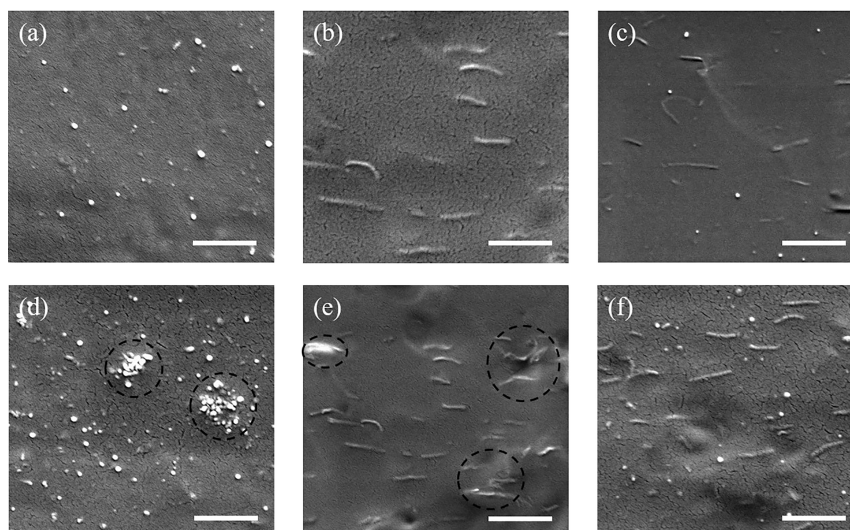
Figure 4. SEM micrographs of (a) 0.6 wt % f-CNT/PVA, (b) 0.6 wt % $Ti_3C_2T_x$/PVA, (c) 0.6 wt % $Ti_3C_2T_x$/f-CNT/PVA, (d) 1.2 wt % f-CNT/ PVA, (e) 1.2 wt % $Ti_3C_2T_x$/PVA, and (f) 1.2 wt % $Ti_3C_2T_x$/f-CNT/PVA. Scale bars, 2 μm.

$Ti_3C_2T_x$/f-CNT hybrids, indicating the formation of hydrogen bonds between the hybrid fillers.[44]

The XRD patterns of pure PVA and PVA nanocomposites are shown in the Supporting Information (Figure S5). Pure PVA shows a characteristic peak at $2\theta \sim 19.6°$ representing reflection from the (101) plane. The XRD patterns of PVA/f-CNT, PVA/$Ti_3C_2T_x$, and PVA/$Ti_3C_2T_x$/f-CNT nanocomposites are similar to the pattern of pure PVA without changes in peak position or intensity. This means that the degree of crystallinity and size of PVA crystals were not affected by the addition of both types of nanomaterials.[32]

The microstructures of the materials were also characterized using scanning electron microscopy. Figure 4 shows the cryo-fractured surfaces of PVA nanocomposite films. As can be seen from Figure 4a, the distribution of f-CNT (bright dots) in the matrix was homogeneous at 0.6 wt % filler loading. Similarly, the distribution of $Ti_3C_2T_x$ (bright lines) in the matrix was also homogeneous at 0.6 wt % filler loading as shown in Figure 4b. The homogeneously distributed f-CNT/$Ti_3C_2T_x$ hybrid could also be observed at the same filler loading (Figure 4c). These results mean that f-CNT, $Ti_3C_2T_x$, or their hybrid could be uniformly dispersed in the matrix at low filler loadings. Carbon nanotube bundles (black circles) were observed when the loading increased to 1.2 wt % (Figure 4d). The restacking of $Ti_3C_2T_x$ nanosheets (black circles) was also observed at 1.2 wt % filler loading (Figure 4e). This is an indication of the difficulties in dispersing the individual nanofillers at this loading homogeneously. In contrast, no bundles or restacking was observed for 1.2 wt % f-CNT/$Ti_3C_2T_x$ hybrid (Figure 4f), indicating a homogeneous dispersion due to the use of the hybrid filler. It should also be noted that the MXene nanoplatelets were fully coated by the polymer, resulting in the alleviation of MXene oxidation.

3.3. Orientation of the Fillers in the Nanocomposites. Figure 5 shows the Raman spectra of pure PVA, PVA/f-CNT, PVA/$Ti_3C_2T_x$, and PVA/$Ti_3C_2T_x$/f-CNT nanocomposites. The spectrum of neat PVA shows a strong peak at ~1368 cm^{-1} due to C−H bending. For PVA/f-CNT films, the spectrum is dominated by the bands of f-CNT (D-band and G-band, respectively). Similarly, for PVA/$Ti_3C_2T_x$ films, the spectrum is dominated by the $Ti_3C_2T_x$ bands. For the PVA/
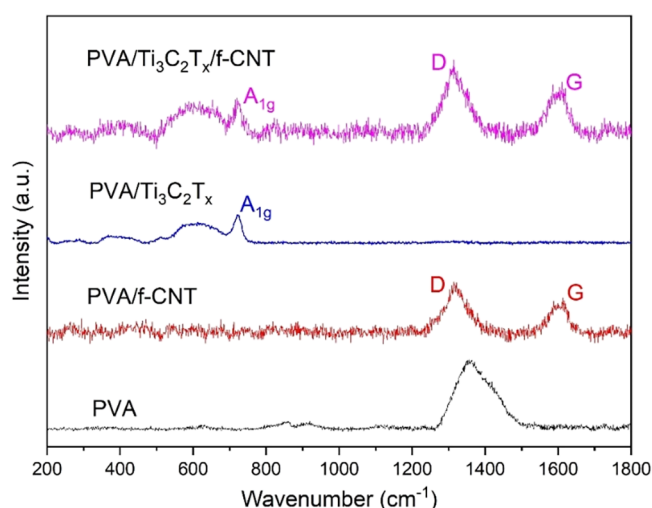
Figure 5. Raman spectra of pure PVA, PVA/f-CNT, PVA/$Ti_3C_2T_x$, and PVA/$Ti_3C_2T_x$/f-CNT nanocomposites. The filler loadings are 1.2 wt % for f-CNT, $Ti_3C_2T_x$, and $Ti_3C_2T_x$/f-CNT.

$Ti_3C_2T_x$/f-CNT ternary nanocomposites, the bands of $Ti_3C_2T_x$ and f-CNT are clearly observed as a result of the strong resonance Raman scatterings of f-CNT and $Ti_3C_2T_x$.

The orientation of the fillers in the nanocomposite films was investigated by polarized Raman spectroscopy. The intensities of the G band of f-CNT and the A_{1g} band of $Ti_3C_2T_x$ were recorded as a function of the rotation angle, as shown in Figure 6. The Raman band intensity is maximum when the nanotube axis is parallel to the incident and scatter laser and minimum when the nanotube axis is perpendicular to the laser polarization.[35] The G-band intensity of nanotube for 1.2 wt % f-CNT/PVA and 1.2 wt % $Ti_3C_2T_x$/f-CNT/PVA did not change significantly with rotation angle within the plane of the films. This suggests that the CNTs were randomly distributed in all directions. The changes in the intensities of A_{1g} band of $Ti_3C_2T_x$ for 1.2 wt % $Ti_3C_2T_x$/PVA and 1.2 wt % $Ti_3C_2T_x$/f-CNT/PVA are shown in Figure 6b,d. In the case of the laser beam being perpendicular to the plane of the film (z), the A_{1g}-band intensity remained unchanged with the rotation angle. When the laser beam was parallel to the plane of the film (x),
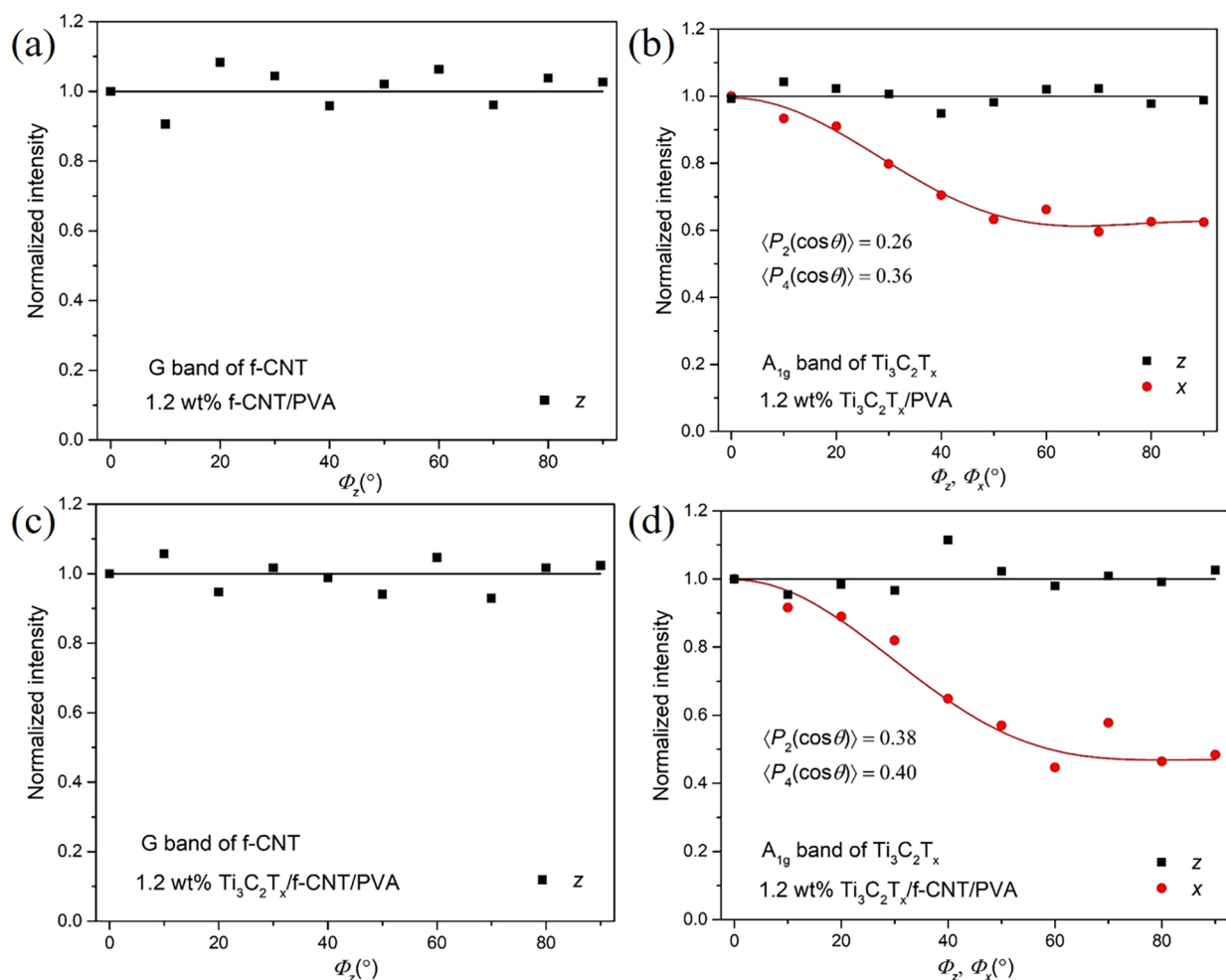
Figure 6. Variation of the normalized intensity of Raman band with rotation angle, (a) G band of f-CNT for 1.2 wt % f-CNT/PVA, (b) A_{1g} band of $Ti_3C_2T_x$ for 1.2 wt % $Ti_3C_2T_x$/PVA, (c) G band of f-CNT for 1.2 wt % $Ti_3C_2T_x$/f-CNT/PVA, and (d) A_{1g} band of $Ti_3C_2T_x$ for 1.2 wt % $Ti_3C_2T_x$/f-CNT/PVA.

the A_{1g}-band intensity was a maximum at 0° and a minimum at 90°. This behavior has been related to the depolarization effect for graphene-like 2D nanosheets.[32] On this basis, the Raman intensity of the sample, $I(\Phi)$, can be expressed by the polarization angle, Φ (Φ_z/Φ_x),as[45]

$$I(\Phi) = I_o\{\frac{8}{15} + \langle P_2(\cos\theta)\rangle(-\frac{16}{21} + \frac{8}{7}\cos^2\Phi)$$
$$+ \langle P_4(\cos\theta)\rangle(\frac{8}{35} - \frac{8}{7}\cos^2\Phi + \cos^4\Phi)\} \quad (1)$$

where I_o is the amplitude and $\langle P_2(\cos\theta)\rangle$ and $\langle P_4(\cos\theta)\rangle$ are fitting parameters. These two parameters are related to the Krenchel orientation factor, η_o, as

$$\eta_o = \frac{8}{15} + \frac{8}{21}\langle P_2(\cos\theta)\rangle + \frac{3}{35}\langle P_4(\cos\theta)\rangle \quad (2)$$

For the fitting of 1.2 wt % $Ti_3C_2T_x$/PVA (Figure 6b), the parameters $\langle P_2(\cos\theta)\rangle = 0.26$ and $\langle P_4(\cos\theta)\rangle = 0.36$ were used, while for the fitting of 1.2 wt % $Ti_3C_2T_x$/f-CNT/PVA (Figure 6d), these two parameters were calculated to be 0.38 and 0.40. The orientation results for PVA nanocomposites with 0.6 wt % f-CNT, $Ti_3C_2T_x$, and $Ti_3C_2T_x$/f-CNT are shown in Figure S6, being similar to the case of 1.2 wt % samples. These results allow the Krenchel orientation factor (η_o) to be

determined. The Krenchel orientation factor for randomly distributed carbon nanotubes in a 2D film was determined to be 3/8.[2] For $Ti_3C_2T_x$, η_o was calculated using eq 2 and the results are summarized in Table 1. The orientation factors were

Table 1. Values of $\langle P_2(\cos\theta)\rangle$, $\langle P_4(\cos\theta)\rangle$ and η_o Determined for Measurements Where the Laser Beam Was Parallel to the Plane of the Film

samples	filler content (wt %)	$\langle P_2(\cos\theta)\rangle$	$\langle P_4(\cos\theta)\rangle$	η_o
$Ti_3C_2T_x$/PVA	0.6	0.25	0.40	0.66
	1.2	0.26	0.36	0.66
$Ti_3C_2T_x$/f-CNT/PVA	0.6	0.40	0.42	0.72
	1.2	0.38	0.40	0.71

the same for 0.6 and 1.2 wt % $Ti_3C_2T_x$/PVA with a value of 0.66. The η_o value increased to 0.72 for 0.6 wt % $Ti_3C_2T_x$/f-CNT/PVA and 0.71 for 1.2 wt % $Ti_3C_2T_x$/f-CNT/PVA, respectively. This suggests that the incorporation of f-CNT promoted the orientation of $Ti_3C_2T_x$ in the plane of the film, induced by strong interfacial interactions between the hybrid fillers.

3.4. Mechanical Properties of PVA/$Ti_3C_2T_x$/f-CNT Films.
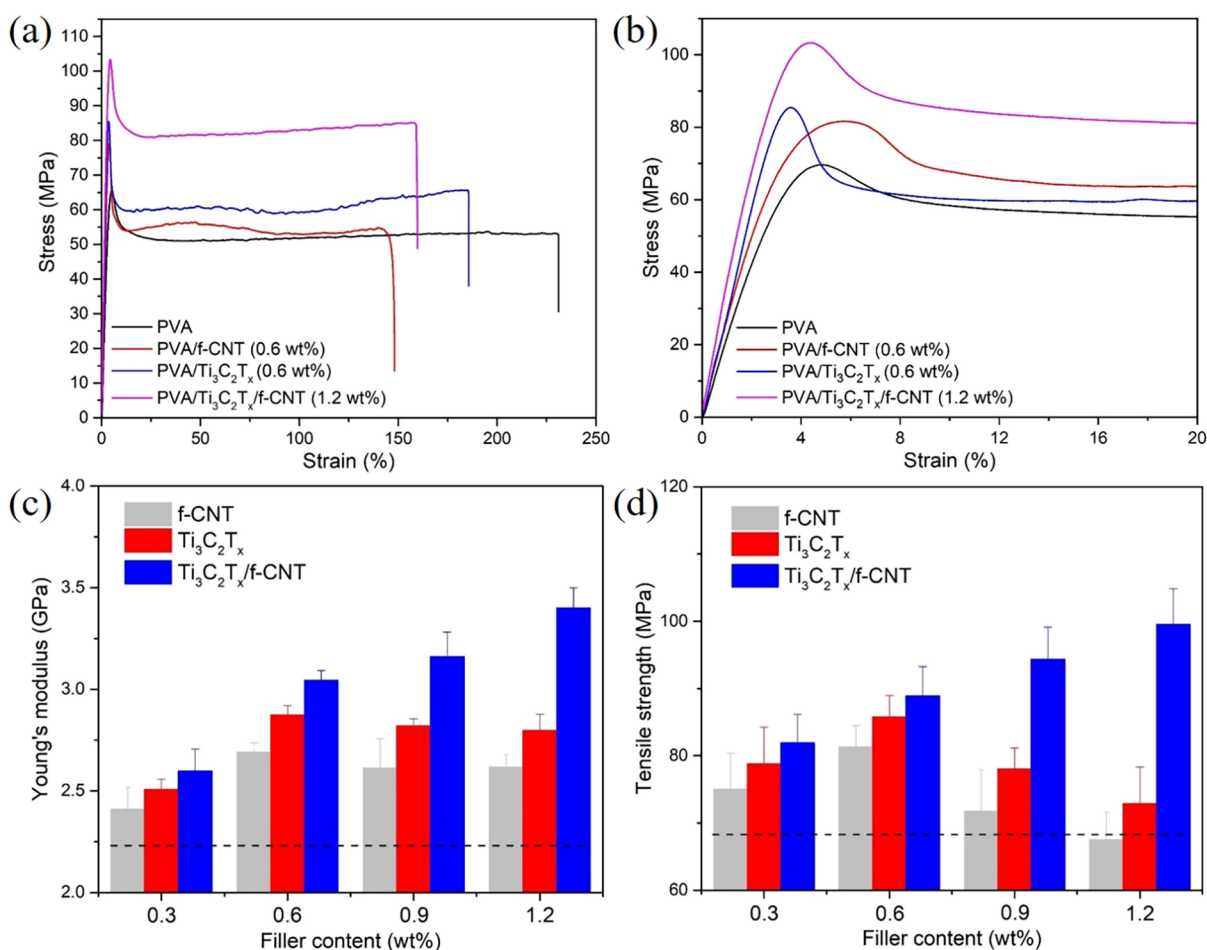Typical stress−strain curves of pure PVA and PVA

Figure 7. (a, b) Stress−strain curves of pure PVA, PVA/f-CNT, PVA/Ti$_3$C$_2$T$_x$, and PVA/Ti$_3$C$_2$T$_x$/f-CNT nanocomposites. Variation of (c) Young's modulus and (d) tensile strength of PVA nanocomposites with filler loading. The black dashed lines represent the Young's modulus and tensile strength of pure PVA.

nanocomposites reinforced by f-CNT, Ti$_3$C$_2$T$_x$, and their hybrids are presented in Figure 7a,b. Both pure PVA and its nanocomposites show distinct yielding and necking behavior. Overall, the Young's modulus and tensile strength were improved despite the low filler loadings, while the fracture strain slightly decreased. The elastic region of the stress−strain curves is presented in Figure S7 in the Supporting Information.

Figure 7c,d shows the variation of Young's modulus and tensile strength of the nanocomposites with increasing filler loadings. The values are also summarized in Table S1 (S8 in the Supporting Information). Young's modulus and tensile strength of pure PVA were 2.23 ± 0.07 GPa 68.3 ± 2.6 MPa, respectively (dashed lines in Figure 7c,d). For PVA/f-CNT and PVA/Ti$_3$C$_2$T$_x$ nanocomposites, the Young's modulus and tensile strength increased up to 0.6 wt % filler loadings. The Young's modulus and tensile strength were improved to 2.69 ± 0.05 GPa and 81.3 ± 3.2 MPa with 0.6 wt % f-CNT and to 2.87 ± 0.05 GPa and 85.8 ± 3.2 MPa with 0.6 wt % Ti$_3$C$_2$T$_x$. After that, Young's modulus and tensile strength showed a downward trend with the increase in filler loading, which was probably induced by poorer dispersion and agglomeration of the fillers as illustrated in Figure 4d,e. Quite interestingly, for the hybrid PVA/Ti$_3$C$_2$T$_x$/f-CNT nanocomposites, Young's modulus and tensile strength increased up to 1.2 wt % filler loading. Young's modulus and tensile strength were improved to 3.4 ± 0.10 GPa and 99.6 ± 5.3 MPa with 1.2 wt % of

Ti$_3$C$_2$T$_x$/f-CNT hybrids. As can be seen from Figure 4f, the Ti$_3$C$_2$T$_x$/f-CNT hybrids showed better dispersion than individual Ti$_3$C$_2$T$_x$ or f-CNT filler, where f-CNTs were dispersed between Ti$_3$C$_2$T$_x$ nanosheets and prevented the agglomeration of Ti$_3$C$_2$T$_x$ nanosheets and CNT entanglements. The contact area between the fillers and the PVA matrix increased, and more hydrogen bonds were formed between the fillers and the matrix, as confirmed by the FTIR spectra. The mechanical properties of the nanocomposites with different weight ratios of Ti$_3$C$_2$T$_x$/f-CNT are summarized in Table S1. After studying three weight ratios (1/2, 1/1, and 2/1), it can be seen that the 1/1 weight ratio of Ti$_3$C$_2$T$_x$/f-CNT hybrids provided the optimum mechanical reinforcement. The DSC curves and degree of crystallinity of PVA and PVA nanocomposites are also shown in Figure S8 and Table S2 in the Supporting Information. The degree of crystallinity of PVA did not change significantly, indicating that the improvements in mechanical properties cannot be ascribed to alterations in crystallinity but rather to the inclusion of nanofillers.

The mechanical properties of PVA composites reinforced with various nanofillers are summarized in Table S3 in the Supporting Information. Clearly, various nanofillers can reinforce PVA effectively at low filler content due to their inherent properties and interfacial interactions with the polymer. Especially graphene oxide, which displays oxygen-containing functional groups, similar to MXene nanoplatelets,

is particularly effective. The use of hybrid fillers offers unique opportunities for advancing PVA nanocomposites toward enhanced performance and multifunctionality while mitigating agglomeration-related challenges. It is worth noting that water absorption can affect the mechanical properties of PVA due to its hydrophilic nature. The effects of water absorption on the interface between the MXene fillers and polymer matrix could be the subject of a future study.

3.5. Modeling of Mechanical Properties of the Nanocomposites.

Young's modulus of a polymer nanocomposite reinforced with an individual filler can be derived from the modified rule of mixtures (ROM)[33]

$$E_c = E_{eff}V_f + E_m(1 - V_f) \tag{3}$$

where E_c and E_m are the Young's modulus of the composite and the matrix, respectively, E_{eff} is the effective Young's modulus of the filler, and V_f is the volume fraction of the filler.

Young's modulus of a polymer nanocomposite with a hybrid filler can be expressed from the extended form of ROM as[46]

$$E_c = E_{eff1}V_{f1} + E_{eff2}V_{f2} + E_m(1 - V_{f1} - V_{f2}) \tag{4}$$

where E_{eff1} and E_{eff2} are the effective Young's moduli of filler 1 and filler 2 and V_{f1} and V_{f2} are the volume fractions of the filler 1 and filler 2, respectively. This equation assumes that no interactions are taking place between the hybrids. The conversion of weight fraction to volume fraction can be found in S11 in the Supporting Information.

The experimental results of Young's modulus and the theoretical prediction from ROM (lines) are shown in Figure 8. For the PVA/Ti$_3$C$_2$T$_x$ nanocomposite, the effective Young's
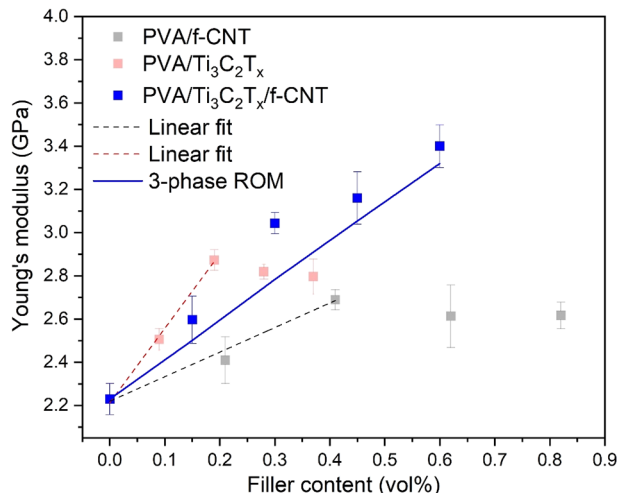

Figure 8. Variation of the Young's modulus of PVA/-f-CNT, PVA/Ti$_3$C$_2$T$_x$, and PVA/Ti$_3$C$_2$T$_x$/f-CNT nanocomposites with the volume fraction of the filler. The experimental results were modeled with the rule of mixtures.

modulus of Ti$_3$C$_2$T$_x$ was determined to be 344.1 GPa. The effective Young's modulus of the filler can also be obtained from $E_{eff} = E_f\eta_o\eta_l$, where η_l is the length factor to evaluate the stress transfer at the filler–matrix interface.[33] If we take the orientation factor of 0.66 as determined earlier and the intrinsic Young's modulus of monolayer Ti$_3$C$_2$T$_x$ (502 GPa from[47]) into this equation, the length factor would equal to ~1. This means that the applied stress was fully transferred to Ti$_3$C$_2$T$_x$ at low loadings. For PVA/f-CNT nanocomposites, the

effective Young's modulus of f-CNT was determined to be 113.7 GPa. If we use the orientation factor of 3/8 and the Young's modulus of carbon nanotubes (1TPa from ref 2) into the above equation and assume full stress transfer, the estimated E_{eff} (375 GPa) would be higher than the value derived from the rule of mixtures. This reduction in the effective Young's modulus of the nanotubes is attributed to the defects induced by acid oxidation and the insufficient interlayer stress transfer efficiency (0.7 from ref 48).

By applying the obtained effective Young's moduli calculated above, the results of the use of the modified ROM for hybrid nanocomposites are also shown in Figure 8. Our experimental results lie above the theoretical prediction, indicating that synergistic effects are taking place between the hybrid components of the system (rather than additive effects arising from zero interactions that the equation assumes). The synergistic effect or percent synergy (%) in mechanical reinforcement due to the use of hybrids of f-CNT and Ti$_3$C$_2$T$_x$ MXene can be obtained from the following equation[49]

$$synergy(\%) = \frac{2pq - (p + q)}{p + q} \times 100 \tag{5}$$

where pq, p, and q are the mechanical properties of the composites with hybrid and individual fillers. Using the above equation, the synergistic effects in Young's modulus of the hybrid PVA/Ti$_3$C$_2$T$_x$/f-CNT nanocomposites with 0.6 and 1.2 wt % filler loadings were calculated to be 23.6 and 22.3%, respectively. The extended ROM for a 3-phase system assumes no interaction between the hybrid fillers, while the Ti$_3$C$_2$T$_x$/f-CNT hybrids were connected through hydrogen bonds, as realized from FTIR. This promoted the homogeneous dispersion of the hybrid fillers in the matrix and improved the orientation of Ti$_3$C$_2$T$_x$ within the matrix (Table 1). At higher loadings, the entanglements of carbon nanotubes and the restacking of Ti$_3$C$_2$T$_x$ nanosheets hinder the stress transfer from the matrix to the fillers. Therefore, the rule of mixtures is not applicable to a 2-phase system when agglomerations occur. In contrast, the tendency to form aggregates was prevented in the 3-phase system as revealed by SEM images (Figure 4). Therefore, our experimental results outperformed the expectations from the modified rule of mixtures, and the synergy between fillers was observed.

3.6. Stress-Induced Raman Band Shifts.

The synergistic reinforcement mechanism was also investigated by strain-induced Raman band shifts. The strain-induced Raman band shifts of f-CNT/PVA, Ti$_3$C$_2$T$_x$/PVA and Ti$_3$C$_2$T$_x$/f-CNT/PVA nanocomposites are shown in Figure 9. The G-band of f-CNT and the A$_{1g}$ band of Ti$_3$C$_2$T$_x$ were monitored to evaluate the stress transfer from PVA to the fillers. For the 1.2 wt % f-CNT/PVA nanocomposite, the shift rate of the G-band was 2.4 ± 0.2 cm^{-1}/% up to 0.4% applied strain. The slippage strain closely resembles the elastic region of the stress–strain curves, as demonstrated in Figure S7 within the Supporting Information. After that, no band shift was observed, which was attributed to interfacial slippage between f-CNTs and PVA. Similar behavior was also observed for 1.2 wt % Ti$_3$C$_2$T$_x$/PVA nanocomposite. The A$_{1g}$ band shift rate was −1.4 ± 0.2 cm^{-1}/% and then slippage occurred at ~ 0.4% applied strain. There were large improvements in the band shift rates for the 1.2 wt % Ti$_3$C$_2$T$_x$/f-CNT/PVA nanocomposite. For example, the G band shift rate of f-CNTs within the hybrid composite was improved to −4.4 ± 0.2 cm^{-1}/%. In addition, slippage
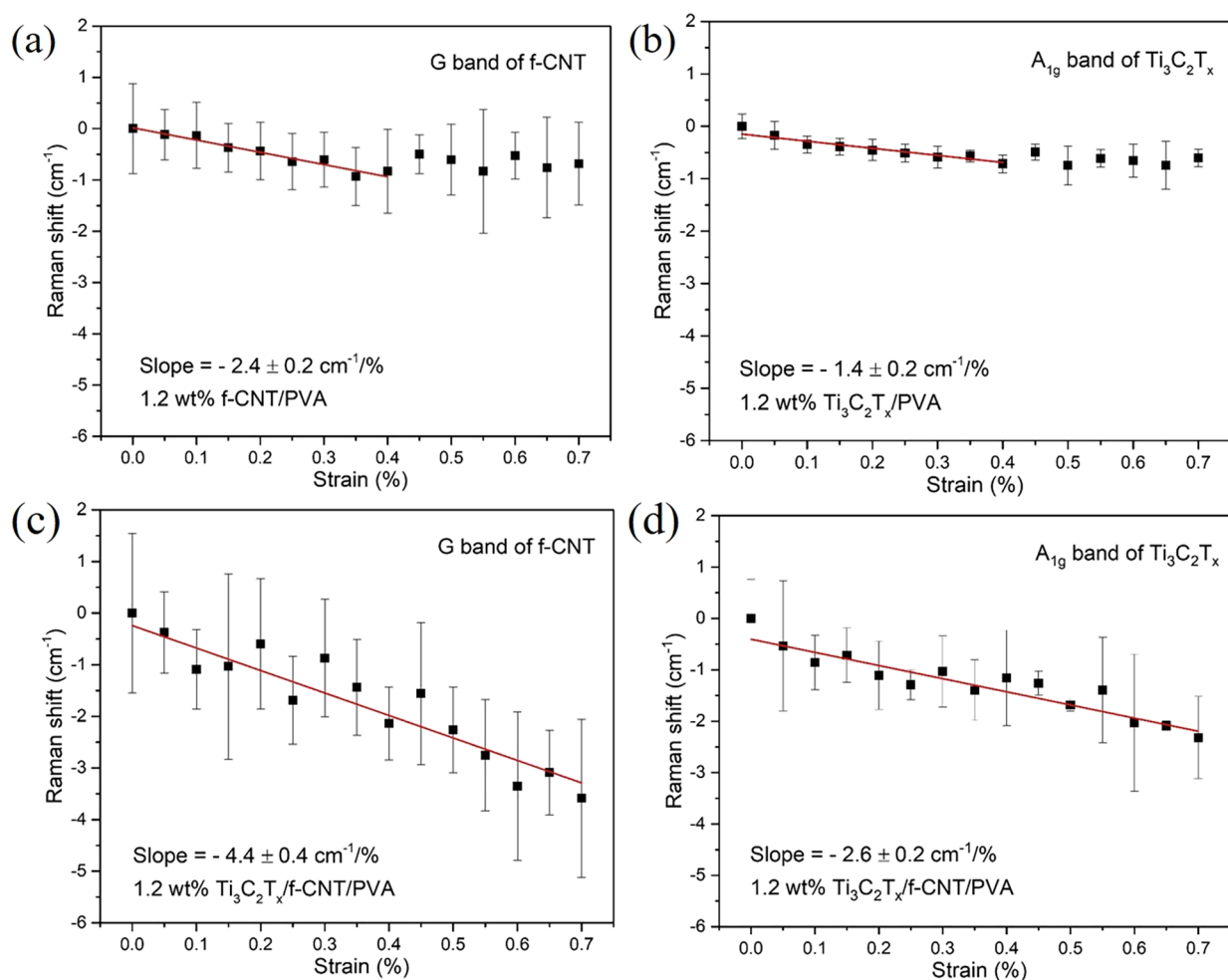
Figure 9. (a) Raman G band shift of f-CNT for 1.2 wt % f-CNT/PVA nanocomposite. (b) Raman A_{1g} band shift of $Ti_3C_2T_x$ for 1.2 wt % $Ti_3C_2T_x$/PVA nanocomposite. (c) Raman G band shift of f-CNT and $Ti_3C_2T_x$/f-CNT/PVA nanocomposite. (d) Raman A_{1g} band shift of $Ti_3C_2T_x$ for 1.2 wt % $Ti_3C_2T_x$/f-CNT/PVA nanocomposite.

occurred at a higher applied strain (0.7%). Similarly, the A_{1g} band shift rate of the $Ti_3C_2T_x$ within the hybrid composite was improved to -2.6 ± 0.2 cm^{-1}/% for $Ti_3C_2T_x$ and slippage occurred again at 0.7% applied strain. This means that stress can be transferred more effectively from PVA to $Ti_3C_2T_x$/f-CNT hybrids. The hybrid nanocomposites can reach higher strains without a reduction in the stress transfer efficiency of the nanofillers, which is another sign of improved dispersion and mitigation of the agglomerates. Similar behavior has been observed for functionalized CNTs,[50] where the functionalization process increased the interfacial adhesion with the PVA matrix and the stress transfer from the matrix to the nanotubes. Functionalized CNTs can activate a more effective stress transfer mechanism, as more hydrogen bonds are formed between the filler and macromolecular chains (in this case, PVA chains), as revealed by FTIR spectra. The same applies for MXene nanoparticles, which display an abundance of functional groups on their surface.

The effective Young's modulus of the fillers can be evaluated from stress-induced Raman band shifts. For carbon nanotubes, the reported reference downshift rate in the G band was about 30 cm^{-1}/%.[51] For $Ti_3C_2T_x$ MXene, the effective modulus, E_{eff}, can be derived from the following equation as

$$E_{eff} = \frac{d\omega_{A_{1g}}}{d\varepsilon} \frac{E_f}{(d\omega_{A_{1g}}/d\varepsilon)_{ref}} \qquad (6)$$

where $d\omega_{A_{1g}}/d\varepsilon$ is the shift rate of the $Ti_3C_2T_x$ Raman A_{1g} mode with strain, the reference shift rate value is taken as -3.7 cm^{-1}/%.[52]

For the 1.2 wt % f-CNT/PVA nanocomposite, the effective Young's modulus of carbon nanotubes was determined to be 80 GPa; for the 1.2 wt % $Ti_3C_2T_x$/PVA nanocomposite, the effective Young's modulus of $Ti_3C_2T_x$ was determined to be 162.8 GPa. In contrast, the effective Young's moduli of carbon nanotubes and $Ti_3C_2T_x$ were determined to be 146.7 and 352.8 GPa, respectively, for 1.2 wt % $Ti_3C_2T_x$/f-CNT/PVA nanocomposites. This suggests that the effective Young's moduli of the fillers were significantly improved within the hybrid nanocomposite. The interfacial interactions between the hybrid filler and the matrix led to a more homogeneous dispersion of the nanomaterials, which in turn increased the contact area between the fillers and PVA matrix. Therefore, stress could be transferred more effectively from the matrix to the fillers, and the mechanical properties were improved.

4. CONCLUSIONS

Herein, ternary PVA/Ti$_3$C$_2$T$_x$/f-CNT nanocomposites were prepared by a simple water casting method. The surface modification of CNTs by acids facilitated their interfacial interactions with Ti$_3$C$_2$T$_x$ MXene, promoting the formation of well-dispersed and three-dimensional Ti$_3$C$_2$T$_x$/f-CNT hybrids in the PVA matrix. The mechanical properties of the ternary nanocomposites were found to be superior to their 2-phase counterparts. For the 1.2 wt % Ti$_3$C$_2$T$_x$/f-CNT hybrids, Young's modulus and tensile strength of pure PVA were improved by 52% and 48%, respectively. The synergistic mechanism was revealed by the use of the modified rule of mixtures and strain-induced Raman band shifts. Stress can be transferred more effectively to the Ti$_3$C$_2$T$_x$/f-CNT hybrids due to the formation of more hydrogen bonds and the homogeneous dispersion of the hybrids within the PVA matrix.

■ ASSOCIATED CONTENT

Ⓢ Supporting Information

The Supporting Information is available free of charge at https://pubs.acs.org/doi/10.1021/acsapm.3c01816.

> Raman spectra, XRD, SEM, AFM, and FTIR of the fillers, XRD of the films, orientation of the fillers, elastic region, mechanical properties and thermal properties of the films, mechanical properties of PVA-based composites, and conversion of weight content to volume content (PDF)

■ AUTHOR INFORMATION

Corresponding Author

Dimitrios G. Papageorgiou − *School of Engineering and Materials Science, Queen Mary University of London, London E1 4NS, United Kingdom*; Email: d.papageorgiou@qmul.ac.uk

Authors

Ming Dong − *School of Physical and Chemical Sciences, Queen Mary University of London, London E1 4NS, United Kingdom*

Yi Hu − *School of Engineering and Materials Science, Queen Mary University of London, London E1 4NS, United Kingdom; School of Mechanical Engineering, Northwestern Polytechnical University, Xi'an 710072, PR China*

Xiangyan Yu − *School of Engineering and Materials Science, Queen Mary University of London, London E1 4NS, United Kingdom;* Ⓞ orcid.org/0000-0002-8203-5754

Mufeng Liu − *Department of Materials, National Graphene Institute, Henry Royce Institute, University of Manchester, Manchester M13 9PL, U.K.;* Ⓞ orcid.org/0000-0002-7671-7804

Emiliano Bilotti − *Department of Aeronautics, Imperial College London, London SW7 2AZ, U.K.;* Ⓞ orcid.org/0000-0003-3952-1148

Han Zhang − *School of Engineering and Materials Science, Queen Mary University of London, London E1 4NS, United Kingdom;* Ⓞ orcid.org/0000-0002-0479-224X

Complete contact information is available at:
https://pubs.acs.org/10.1021/acsapm.3c01816

Notes

The authors declare no competing financial interest.

■ ACKNOWLEDGMENTS

■ REFERENCES

(1) Li, Y. C.; Huang, X. R.; Zeng, L. J.; Li, R. F.; Tian, H. F.; Fu, X. W.; Wang, Y.; Zhong, W. H. A review of the electrical and mechanical properties of carbon nanofiller-reinforced polymer composites. *J. Mater. Sci.* **2019**, *54* (2), 1036−1076.

(2) Papageorgiou, D. G.; Li, Z. L.; Liu, M. F.; Kinloch, I. A.; Young, R. J. Mechanisms of mechanical reinforcement by graphene and carbon nanotubes in polymer nanocomposites. *Nanoscale* **2020**, *12* (4), 2228−2267.

(3) Dong, M.; Young, R. J.; Dunstan, D. J.; Papageorgiou, D. G. Interfacial stress transfer in monolayer and few-layer MoS$_2$ nanosheets in model nanocomposites. *Compos. Sci. Technol.* **2023**, *233*, No. 109892.

(4) Dong, M.; Zhang, H.; Tzounis, L.; Santagiuliana, G.; Bilotti, E.; Papageorgiou, D. G. Multifunctional epoxy nanocomposites reinforced by two-dimensional materials: A review. *Carbon* **2021**, *185*, 57−81.

(5) VahidMohammadi, A.; Rosen, J.; Gogotsi, Y. The world of two-dimensional carbides and nitrides (MXenes). *Science* **2021**, *372* (6547), 1165.

(6) Shekhirev, M.; Shuck, C. E.; Sarycheva, A.; Gogotsi, Y. Characterization of MXenes at every step, from their precursors to single flakes and assembled films. *Prog. Mater. Sci.* **2021**, *120*, No. 100757.

(7) Riazi, H.; Nemani, S. K.; Grady, M. C.; Anasori, B.; Soroush, M. Ti$_3$C$_2$ MXene-polymer nanocomposites and their applications. *J. Mater. Chem. A* **2021**, *9* (13), 8051−8098.

(8) Wan, S.; Li, X.; Chen, Y.; Liu, N.; Wang, S.; Du, Y.; Xu, Z.; Deng, X.; Dou, S.; Jiang, L.; Cheng, Q. Ultrastrong MXene films via the synergy of intercalating small flakes and interfacial bridging. *Nat. Commun.* **2022**, *13* (1), 7340.

(9) Sanes, J.; Sánchez, C.; Pamies, R.; Avilés, M.-D.; Bermúdez, M.-D. Extrusion of Polymer Nanocomposites with Graphene and Graphene Derivative Nanofillers: An Overview of Recent Developments. *Materials* **2020**, *13* (3), 549.

(10) Wan, S.; Li, X.; Wang, Y.; Chen, Y.; Xie, X.; Yang, R.; Tomsia, A. P.; Jiang, L.; Cheng, Q. Strong sequentially bridged MXene sheets. *Proc. Natl. Acad. Sci. U. S. A.* **2020**, *117* (44), 27154−27161.

(11) Wan, S.; Li, X.; Chen, Y.; Liu, N.; Du, Y.; Dou, S.; Jiang, L.; Cheng, Q. High-strength scalable MXene films through bridging-induced densification. *Science* **2021**, *374* (6563), 96−99.

(12) Wan, S.; Chen, Y.; Fang, S.; Wang, S.; Xu, Z.; Jiang, L.; Baughman, R. H.; Cheng, Q. High-strength scalable graphene sheets by freezing stretch-induced alignment. *Nat. Mater.* **2021**, *20* (5), 624−631.

(13) Huang, X.; Zhi, C.; Jiang, P. Toward Effective Synergetic Effects from Graphene Nanoplatelets and Carbon Nanotubes on Thermal Conductivity of Ultrahigh Volume Fraction Nanocarbon Epoxy Composites. *J. Phys. Chem. C* **2012**, *116* (44), 23812−23820.

(14) Cataldi, P.; Steiner, P.; Raine, T.; Lin, K.; Kocabas, C.; Young, R. J.; Bissett, M.; Kinloch, I. A.; Papageorgiou, D. G. Multifunctional Biocomposites Based on Polyhydroxyalkanoate and Graphene/Carbon Nanofiber Hybrids for Electrical and Thermal Applications. *ACS Appl. Polym. Mater.* **2020**, *2* (8), 3525−3534.

(15) Wan, S.; Xu, F.; Jiang, L.; Cheng, Q. Superior Fatigue Resistant Bioinspired Graphene-Based Nanocomposite via Synergistic Interfacial Interactions. *Adv. Funct. Mater.* **2017**, *27* (10), 1605636.

(16) Zhang, Y. Y.; Gong, S. S.; Zhang, Q.; Ming, P.; Wan, S. J.; Peng, J. S.; Jiang, L.; Cheng, Q. F. Graphene-based artificial nacre nanocomposites. *Chem. Soc. Rev.* **2016**, *45* (9), 2378−2395.

(17) Szeluga, U.; Kumanek, B.; Trzebicka, B. Synergy in hybrid polymer/nanocarbon composites. A review. *Compos. Pt. A-Appl. Sci. Manuf.* **2015**, *73*, 204−231.

(18) Wan, S. J.; Peng, J. S.; Li, Y. C.; Hu, H.; Jiang, L.; Cheng, Q. F. Use of Synergistic Interactions to Fabricate Strong, Tough, and Conductive Artificial Nacre Based on Graphene Oxide and Chitosan. *ACS Nano* **2015**, *9* (10), 9830−9836.

(19) Li, Y. Q.; Yang, T. Y.; Yu, T.; Zheng, L. X.; Liao, K. Synergistic effect of hybrid carbon nantube-graphene oxide as a nanofiller in enhancing the mechanical properties of PVA composites. *J. Mater. Chem.* **2011**, *21* (29), 10844−10851.

(20) Zhang, C.; Huang, S.; Tjiu, W. W.; Fan, W.; Liu, T. X. Facile preparation of water-dispersible graphene sheets stabilized by acid-treated multi-walled carbon nanotubes and their poly(vinyl alcohol) composites. *J. Mater. Chem.* **2012**, *22* (6), 2427−2434.

(21) Wang, J. F.; Jin, X. X.; Wu, H.; Guo, S. Y. Polyimide reinforced with hybrid graphene oxide @ carbon nanotube: Toward high strength, toughness, electrical conductivity. *Carbon* **2017**, *123*, 502−513.

(22) Gong, S. S.; Cui, W.; Zhang, Q.; Cao, A. Y.; Jiang, L.; Cheng, Q. F. Integrated Ternary Bioinspired Nanocomposites via Synergistic Toughening of Reduced Graphene Oxide and Double-Walled Carbon Nanotubes. *ACS Nano* **2015**, *9* (12), 11568−11573.

(23) Oh, J. Y.; Kim, Y. S.; Jung, Y.; Yang, S. J.; Park, C. R. Preparation and Exceptional Mechanical Properties of Bone-Mimicking Size-Tuned Graphene Oxide@Carbon Nanotube Hybrid Paper. *ACS Nano* **2016**, *10* (2), 2184−2192.

(24) Akter, R.; Jeong, B.; Choi, J.-S.; Rahman, M. A. Ultrasensitive Nanoimmunosensor by coupling non-covalent functionalized graphene oxide platform and numerous ferritin labels on carbon nanotubes. *Biosens. Bioelectron.* **2016**, *80*, 123−130.

(25) Liu, X.; Miller, A. L., II; Park, S.; Waletzki, B. E.; Terzic, A.; Yaszemski, M. J.; Lu, L. Covalent crosslinking of graphene oxide and carbon nanotube into hydrogels enhances nerve cell responses. *J. Mater. Chem. B* **2016**, *4* (43), 6930−6941.

(26) Cheng, Q.; Duan, J.; Zhang, Q.; Jiang, L. Learning from Nature: Constructing Integrated Graphene-Based Artificial Nacre. *ACS Nano* **2015**, *9* (3), 2231−2234.

(27) Atif, R.; Inam, F. Reasons and remedies for the agglomeration of multilayered graphene and carbon nanotubes in polymers. *Beilstein J. Nanotechnol.* **2016**, *7*, 1174−1196.

(28) Aakyiir, M.; Oh, J. A.; Araby, S.; Zheng, Q.; Naeem, M.; Ma, J.; Adu, P.; Zhang, L.; Mai, Y. W. Combining hydrophilic MXene nanosheets and hydrophobic carbon nanotubes for mechanically resilient and electrically conductive elastomer nanocomposites. *Compos. Sci. Technol.* **2021**, *214*, No. 108997.

(29) Wang, Y. F.; Liang, L. Y.; Du, Z. R.; Wang, Y. M.; Liu, C. T.; Shen, C. Y. Biodegradable PLA/CNTs/Ti$_3$C$_2$T$_x$ MXene nanocomposites for efficient electromagnetic interference shielding. *J. Mater. Sci.-Mater. Electron.* **2021**, *32* (21), 25952−25962.

(30) Alhabeb, M.; Maleski, K.; Anasori, B.; Lelyukh, P.; Clark, L.; Sin, S.; Gogotsi, Y. Guidelines for Synthesis and Processing of Two-Dimensional Titanium Carbide (Ti$_3$C$_2$T$_X$ MXene). *Chem. Mater.* **2017**, *29* (18), 7633−7644.

(31) Datsyuk, V.; Kalyva, M.; Papagelis, K.; Parthenios, J.; Tasis, D.; Siokou, A.; Kallitsis, I.; Galiotis, C. Chemical oxidation of multiwalled carbon nanotubes. *Carbon* **2008**, *46* (6), 833−840.

(32) Li, Z.; Young, R. J.; Kinloch, I. A. Interfacial Stress Transfer in Graphene Oxide Nanocomposites. *ACS Appl. Mater. Interfaces* **2013**, *5* (2), 456−463.

(33) Young, R. J.; Liu, M. F.; Kinloch, I. A.; Li, S. H.; Zhao, X.; Valles, C.; Papageorgiou, D. G. The mechanics of reinforcement of polymers by graphene nanoplatelets. *Compos. Sci. Technol.* **2018**, *154*, 110−116.

(34) Hao, S.; Li, Z.; Yang, C.; Marsden, A. J.; Kinloch, I. A.; Young, R. J. Interfacial energy dissipation in bio-inspired graphene nanocomposites. *Compos. Sci. Technol.* **2022**, *219*, No. 109216.

(35) Deng, L.; Eichhorn, S. J.; Kao, C.-C.; Young, R. J. The Effective Young's Modulus of Carbon Nanotubes in Composites. *ACS Appl. Mater. Interfaces* **2011**, *3* (2), 433−440.

(36) Sarycheva, A.; Gogotsi, Y. Raman Spectroscopy Analysis of the Structure and Surface Chemistry of Ti$_3$C$_2$T$_x$ MXene. *Chem. Mater.* **2020**, *32* (8), 3480−3488.

(37) Dresselhaus, M. S.; Dresselhaus, G.; Saito, R.; Jorio, A. Raman spectroscopy of carbon nanotubes. *Phys. Rep.* **2005**, *409* (2), 47−99.

(38) Osswald, S.; Havel, M.; Gogotsi, Y. Monitoring oxidation of multiwalled carbon nanotubes by Raman spectroscopy. *J. Raman Spectrosc.* **2007**, *38* (6), 728−736.

(39) Saleh, T. A. The influence of treatment temperature on the acidity of MWCNT oxidized by HNO$_3$ or a mixture of HNO$_3$/H$_2$SO$_4$. *Appl. Surf. Sci.* **2011**, *257* (17), 7746−7751.

(40) Wang, L.; Chen, L. X.; Song, P.; Liang, C. B.; Lu, Y. J.; Qiu, H.; Zhang, Y. L.; Kong, J.; Gu, J. W. Fabrication on the annealed Ti$_3$C$_2$T$_x$ MXene/Epoxy nanocomposites for electromagnetic interference shielding application. *Compos. Pt. B-Eng.* **2019**, *171*, 111−118.

(41) Cao, Y.; Deng, Q.; Liu, Z.; Shen, D.; Wang, T.; Huang, Q.; Du, S.; Jiang, N.; Lin, C.-T.; Yu, J. Enhanced thermal properties of poly(vinylidene fluoride) composites with ultrathin nanosheets of MXene. *RSC Adv.* **2017**, *7* (33), 20494−20501.

(42) Chiang, Y.-C.; Lin, W.-H.; Chang, Y.-C. The influence of treatment duration on multi-walled carbon nanotubes functionalized by H$_2$SO$_4$/HNO$_3$ oxidation. *Appl. Surf. Sci.* **2011**, *257* (6), 2401−2410.

(43) Zhang, X.; Liu, W.; Liu, W.; Qiu, X. High performance PVA/lignin nanocomposite films with excellent water vapor barrier and UV-shielding properties. *Int. J. Biol. Macromol.* **2020**, *142*, 551−558.

(44) Núñez, J. D.; Benito, A. M.; Rouzière, S.; Launois, P.; Arenal, R.; Ajayan, P. M.; Maser, W. K. Graphene oxide−carbon nanotube hybrid assemblies: cooperatively strengthened OH···O = C hydrogen bonds and the removal of chemisorbed water. *Chem. Sci.* **2017**, *8* (7), 4987−4995.

(45) Li, Z. L.; Young, R. J.; Wilson, N. R.; Kinloch, I. A.; Valles, C.; Li, Z. Effect of the orientation of graphene-based nanoplatelets upon the Young's modulus of nanocomposites. *Compos. Sci. Technol.* **2016**, *123*, 125−133.

(46) Papageorgiou, D. G.; Kinloch, I. A.; Young, R. J. Hybrid multifunctional graphene/glass-fibre polypropylene composites. *Compos. Sci. Technol.* **2016**, *137*, 44−51.

(47) Borysiuk, V. N.; Mochalin, V. N.; Gogotsi, Y. Molecular dynamic study of the mechanical properties of two-dimensional titanium carbides Ti$_{n+1}$C$_n$ (MXenes). *Nanotechnology* **2015**, *26* (26), No. 265705.

(48) Young, R. J.; Deng, L.; Wafy, T. Z.; Kinloch, I. A. Interfacial and internal stress transfer in carbon nanotube based nanocomposites. *J. Mater. Sci.* **2016**, *51* (1), 344−352.

(49) Duan, J. L.; Gong, S. S.; Gao, Y.; Xie, X. L.; Jiang, L.; Cheng, Q. F. Bioinspired Ternary Artificial Nacre Nanocomposites Based on Reduced Graphene Oxide and Nanofibrillar Cellulose. *ACS Appl. Mater. Interfaces* **2016**, *8* (16), 10545−10550.

(50) Liu, L. Q.; Barber, A. H.; Nuriel, S.; Wagner, H. D. Mechanical properties of functionalized single-walled carbon-nanotube/poly(vinyl alcohol) nanocomposites. *Adv. Funct. Mater.* **2005**, *15* (6), 975−980.

(51) Cronin, S. B.; Swan, A. K.; Ünlü, M. S.; Goldberg, B. B.; Dresselhaus, M. S.; Tinkham, M. Measuring the Uniaxial Strain of Individual Single-Wall Carbon Nanotubes: Resonance Raman Spectra of Atomic-Force-Microscope Modified Single-Wall Nanotubes. *Phys. Rev. Lett.* **2004**, *93* (16), No. 167401.

(52) Liu, M. F.; Zhuo, Y. L.; Sarycheva, A.; Gogotsi, Y.; Bissett, M. A.; Young, R. J.; Kinloch, I. A. Deformation of and Interfacial Stress Transfer in Ti$_3$C$_2$ MXene-Polymer Composites. *ACS Appl. Mater. Interfaces* **2022**, *14* (8), 10681−10690.